Catalysis Science & Technology

ROYAL SOCIETY OF CHEMISTRY

PAPER

View Article Online
View Journal | View Issue

Cite this: *Catal. Sci. Technol.*, 2025, 15, 3848

Unveiling intrinsic active sites and pivotal intermediate species in N_2O decomposition over Co_3O_4-based catalysts†

Yihuai Zhang,‡[a] Qi Dong,‡[b] Jianning Zhang,[ca] Tao Zhang *[a] and Junhua Li [d]

Received 27th March 2025,
Accepted 15th May 2025

DOI: 10.1039/d5cy00381d

rsc.li/catalysis

Identifying active sites and reaction intermediates in N_2O decomposition remains a key challenge for spinel-based catalysts. Here, we developed Cu-doped Co_3O_4 catalysts with remarkable N_2O decomposition performance by precisely tuning their surface composition and redox properties. Through a combined experimental and theoretical approach, we identified the "⊡-Co^{2+}" pair, comprising a Co^{2+} cation and an adjacent oxygen vacancy (⊡), as the intrinsic active site driving the catalytic process. Crucially, *in situ* DRIFTS provided the first direct evidence of *trans*-$N_2O_2^-$ as a pivotal reaction intermediate, representing a significant breakthrough in understanding the catalytic mechanism. Based on these insights, we propose a detailed pathway where N_2O adsorbs and dissociates on the Co^{2+} site, while dissociated oxygen undergoes spillover to the vacancy, facilitating the formation of *trans*-$N_2O_2^-$ and driving the catalytic cycle to completion. This unprecedented discovery clarifies the structure–activity relationship in spinel oxides and provides a robust foundation for designing advanced catalysts for N_2O abatement and beyond.

1. Introduction

Nitrous oxide (N_2O), a potent greenhouse gas with a global warming potential approximately 300 times that of carbon dioxide, is also a significant contributor to stratospheric ozone depletion.[1,2] As the third most impactful anthropogenic greenhouse gas, N_2O emissions have steadily increased due to industrial activities, agriculture, and fossil fuel combustion, posing severe environmental and climatic threats.[1,3,4] The direct catalytic decomposition of N_2O into nitrogen and oxygen is widely regarded as one of the most efficient and environmentally benign strategies for mitigating its emissions.[5] This process offers a distinct advantage over alternative methods, such as selective catalytic reduction (SCR), by circumventing the need for reducing agents, thereby simplifying the process and enhancing sustainability.

Over the past decades, a variety of catalysts, including noble-metal-supported systems,[6–8] metal oxides,[9–11] and zeolite-based materials,[12–14] have been developed for N_2O decomposition. Among these, cobalt oxide (Co_3O_4), a spinel-structured material characterized by its mixed-valence states, tetrahedral Co^{2+} in the A site and octahedral Co^{3+} in the B site, has emerged as a highly promising candidate.[15–17] The exceptional catalytic performance of Co_3O_4 is attributed to its unique electronic structure, which facilitates redox flexibility, oxygen mobility, and the formation of reactive oxygen species.[1,17] Furthermore, doping strategies involving the substitution of elements into the A or B sites of Co_3O_4 have been shown to significantly enhance its catalytic activity by modulating redox properties, increasing oxygen vacancy concentrations, and improving N_2O adsorption and activation.[16,18–22] These advancements have propelled Co_3O_4-based catalysts to the forefront of N_2O decomposition research.

Despite these achievements, fundamental challenges remain in elucidating the reaction mechanism of N_2O decomposition. Two primary mechanisms, Langmuir–Hinshelwood (L–H) and Eley–Rideal (E–R), have been proposed to describe the reaction.[23–25] In the L–H mechanism, N_2O adsorbs onto the catalyst surface (R1), dissociates into nitrogen gas (N_2) and adsorbed oxygen species (O*) (R2), followed by recombination of O* species to release O_2 (R3). In contrast, the E–R mechanism involves the direct reaction of a gas-phase N_2O molecule with an adsorbed

[a] *School of Chemistry and Life Resources, Renmin University of China, Beijing, 100872, P. R. China. E-mail: zhangt@ruc.edu.cn*
[b] *College of Chemistry and Chemical Engineering, Taiyuan University of Technology, Taiyuan, 030024, P. R. China*
[c] *College of Science, China University of Petroleum, Beijing, 102249, P. R. China*
[d] *State Key Joint Laboratory of Environment Simulation and Pollution Control, School of Environment, Tsinghua University, Beijing, 100084, P. R. China*

† Electronic supplementary information (ESI) available. See DOI: https://doi.org/10.1039/d5cy00381d

‡ Y. Z. and Q. D. contributed equally to this work.

O* species to produce N_2 and O_2 (R4). While these models provide a foundational understanding, their oversimplification and lack of direct experimental evidence for transient intermediates limit their applicability to real-world systems.

$$N_2O(g) + *(\text{surface active site}) \leftrightarrow N_2O^* \quad (R1)$$

$$N_2O^* \rightarrow N_2(g) + O^* \quad (R2)$$

$$O^* + O^* \leftrightarrow O_2(g) + 2^* \text{ (L–H mechanism)} \quad (R3)$$

$$N_2O(g) + O^* \rightarrow N_2(g) + O_2(g) + * \text{ (E–R mechanism)} \quad (R4)$$

The nature of active sites further complicates mechanistic studies. For Co_3O_4-based catalysts, both tetrahedral Co^{2+} and octahedral Co^{3+} have been proposed as potential active sites.[15,26] While Co^{2+} is often associated with the L–H mechanism, Co^{3+} is linked to the E–R pathway.[22,27,28] The coexistence of these active sites and the dynamic restructuring of the catalyst surface under reaction conditions introduce further uncertainty.[29] Identifying the intrinsic active sites and key transient intermediates, as well as correlating them with specific mechanistic pathways is therefore critical to resolving these controversies.

To address these challenges, this study combines *in situ* diffuse reflectance infrared Fourier transform spectroscopy (*in situ* DRIFTS), kinetic studies, and density functional theory (DFT) calculations to establish a comprehensive understanding of the N_2O decomposition mechanism on Cu-doped Co_3O_4 spinel catalysts, prepared *via* typical A-site substitution. By integrating experimental observations with theoretical modeling, we aim to (1) unambiguously identify the intrinsic active sites, (2) detect and characterize key transient intermediates, and (3) elucidate the detailed reaction pathway. Notably, we present the first direct evidence of surface-bound $N_2O_2^-$ as a critical transient intermediate, identified using *in situ* DRIFTS, thereby providing mechanistic insights into the catalytic process. Furthermore, the influence of Cu doping on the electronic structure, oxygen vacancy formation, and overall catalytic performance is systematically investigated. These findings contribute to a deeper understanding of the structure–activity relationship and offer valuable guidance for the rational design of next-generation catalysts for N_2O mitigation.

2. Experimental section

2.1 Catalyst preparation

Cu-doped Co_3O_4 catalysts were synthesized *via* a co-precipitation method using sodium carbonate (Na_2CO_3) as the precipitating agent. Stoichiometric amounts of cobalt nitrate hexahydrate ($Co(NO_3)_2{\cdot}6H_2O$) and copper nitrate hexahydrate ($Cu(NO_3)_2{\cdot}3H_2O$) were dissolved in deionized water to form a homogeneous 0.4 mol L^{-1} aqueous solution. This precursor solution was stirred continuously for 1 hour, during which a 1 mol L^{-1} Na_2CO_3 solution was gradually added dropwise. The addition was controlled to maintain a uniform pH increase, and the final pH was adjusted to 9.3, a condition optimized to ensure complete precipitation while minimizing the formation of undesirable by-products.

The resulting precipitate was collected by filtration and thoroughly washed with deionized water to remove residual ions. It was then dried at 110 °C for 3 hours in an air atmosphere to remove moisture. Subsequently, the dried precursor was calcined at 550 °C for 3 hours in air to produce the final catalysts. The prepared catalysts are denoted as Cu_x-CoO_y, where "x" corresponds to the molar ratio of Cu to Co, and "y" represents the oxygen stoichiometry influenced by doping.

For comparative studies, bare Co_3O_4 and CuO catalysts were synthesized following the same co-precipitation protocol, ensuring consistent experimental conditions for meaningful performance comparisons.

2.2 Characterization methods

Textural analyses were conducted using a TriStar II 3020 analyzer (Micromeritics). X-ray powder diffraction (XRD) patterns were recorded on a SmartLab (3 kW) diffractometer (Rigaku) equipped with a Cu Kα radiation source. The surface morphologies of the samples were examined using scanning electron microscopy (SEM, SU8010, Hitachi). Transmission electron microscopy (TEM) images were captured using a JEOL JEM-2100F electron microscope operating at an acceleration voltage of 200 kV. Raman spectra were collected using a Renishaw RM2000 Raman spectrometer with a laser wavelength of 532 nm. X-ray photoelectron spectroscopy (XPS) was performed using a Thermo ESCALAB 250XI spectrometer with an Al Kα excitation source operating at 150 W. The binding energy scale was calibrated using the C 1s peak at 284.8 eV.

Hydrogen temperature-programmed reduction (H_2-TPR) experiments were carried out on a Micromeritics AutoChem II 2920 instrument. Pre-treatment was conducted under helium by heating the sample from room temperature to 300 °C at a rate of 10 °C min^{-1}, followed by purging at 300 °C for 1 hour. After cooling to room temperature, the carrier gas was switched to 10 vol% H_2/Ar and purged for 1 hour. Once the baseline stabilized, the temperature was increased to 900 °C at a ramp rate of 10 °C min^{-1}, and the consumption was recorded.

In situ diffuse reflectance infrared Fourier transform spectroscopy (*in situ* DRIFTS) was conducted on a Bruker INVENIO S spectrometer equipped with a liquid nitrogen-cooled mercury cadmium telluride (MCT) detector. For each test, approximately 0.08 g of catalyst was uniformly packed in a high-temperature reaction cell. Prior to the experiment, catalyst powders were calcined at 500 °C for 1 hour under a continuous flow of air. After activation, the sample was cooled to the desired reaction temperature, and a background spectrum was recorded. Subsequently, a gas

mixture containing 500 ppm N_2O balanced with Ar was continuously introduced at a flow rate of 50 mL min^{-1} throughout the measurements, and spectra were then collected at a resolution of 4 cm^{-1} with 100 scans per spectrum to monitor the reaction intermediates in real time.

2.3 Activity test and kinetic studies

Catalytic activity tests were performed in a fixed-bed quartz reactor to evaluate the N_2O decomposition performance of the catalysts. A gas mixture containing 500 ppm N_2O balanced with Ar was introduced into the reactor at a flow rate of 200 mL min^{-1}, with 0.1 g of catalyst loaded in the reactor. The resulting gas hourly space velocity (GHSV) was 120 000 h^{-1}. The concentration of N_2O in the inlet and outlet streams was continuously monitored using an online FT-IR gas analyzer (Antaris IGS). The N_2O conversion (X_{N_2O}) was calculated using eqn (1):

$$X_{N_2O}\,(\%) = \frac{[N_2O]_{in} - [N_2O]_{out}}{[N_2O]_{in}} \quad (1)$$

Steady-state kinetic studies of N_2O decomposition were conducted under the same conditions. The reactant gas contained 100–700 ppm N_2O balanced with Ar, with GHSV values ranging from 120 000 to 1 200 000 h^{-1}. High GHSV values were employed to maintain N_2O conversion below 15%, thereby minimizing potential diffusion limitations and ensuring intrinsic kinetic control. The reaction rate (r_{N_2O}, mol N_2O g^{-1} min^{-1}) was calculated using eqn (2):

$$r_{N_2O} = \frac{F \times X_{N_2O} \times [N_2O]_{in}}{V_m \times m_{cat}} \quad (2)$$

where F is the total mole flow rate (mL min^{-1}). V_m is the gas molar volume (22 400 cm^3), m_{cat} represents the mass of the catalysts (g).

2.4 Molecular modeling

Previous experimental data suggest that the Co_3O_4 spinel predominantly exposes the (100) and (111) planes, with minimal exposure of the (110) plane. Additionally, the (100) plane is more stable than the (110) and (111) planes in a wide range of temperatures.[30–32] Therefore, the Co_3O_4 (100) was modeled using a [2 × 2] supercell to construct the slab model (Fig. S1a†), Cu-doped Co_3O_4 (100) was built by replacing a Co^{2+} with Cu^{2+} (Fig. S1b†).

The plane wave-based pseudo-potential code was implemented in the Vienna *ab initio* simulation package (VASP).[33,34] Electron–ion interaction was described by the projector augmented wave method (PAW).[35,36] The Perdew, Burke, and Ernzerhof functional within the generalized gradient approximation (GGA-PBE)[37] plus Hubbard model (GGA + U) was used to calculate the electronic exchange and correlation. The Ueff of Cu and Co in this study were 7.0 and 3.5 eV, respectively.[38,39] PBE-D3 parameter of Grimme *et al.* was used to perform dispersion correction.[40] The cutoff energy of the plane wave is 500 eV.[41–43] To deal with the orbitals occupied by the fractions near the Fermi level and the energy level broadening, we used the Gaussian smearing method with σ = 0.05 eV. The convergence criteria for electron and ion steps are 10^{-5} eV in total energy and 0.03 eV $Å^{-1}$ in force. A 3 × 3 × 1 Monkhorst–Pack k-point grids was used for sampling the Brillouin zone. The top and bottom three layers of the slab models were released and middle layers are fixed. The thickness of the slab was ~15 Å, with a 15 Å vacuum gap.

The adsorption energies (E_{ads}) were calculated as $E_{ads} = E_{ad/sub} - E_{ad} - E_{sub}$, ($E_{ad/sub}$, E_{ad}, and E_{sub} are the total energies of the optimized adsorbate/substrate system, the adsorbate, and the clean substrate, respectively). The climbing image nudged elastic band (CI-NEB) method was employed to determine the transition states. According to the reaction condition, we included entropy contribution and computed the Gibbs free energies at 350 °C.

3. Results and discussion

3.1 Catalytic performance

The catalytic performance of the synthesized catalysts for N_2O decomposition was evaluated, and the results are presented in Fig. 1a. The bare Co_3O_4 catalyst exhibited limited activity, achieving less than 90% N_2O conversion even at 500 °C. Upon doping Co_3O_4 with Cu, the catalytic activity was significantly enhanced. A volcanic relationship was observed between Cu content and catalytic performance, with $Cu_{0.15}CoO_y$ achieving nearly 100% N_2O conversion at a much lower temperature of 425 °C. This result highlights the crucial role of Cu doping in enhancing the catalytic performance of Co_3O_4. Interestingly, bare CuO displayed poor catalytic activity, with only 4% N_2O conversion at 425 °C. This stark contrast suggests that Cu alone does not act as the primary active phase for N_2O decomposition. Instead, Cu appears to function more as a promoter in the Cu-doped Co_3O_4 system, interacting with Co_3O_4 to enhance its catalytic properties. Additionally, a 12-hour stability test at 400 °C (Fig. S2a†) showed negligible activity loss (>99% conversion maintained), demonstrating excellent durability. Multiple cycling tests (Fig. S2b†) also confirmed robust stability, with activity variation less than 3% over three consecutive cycles.

The effect of O_2, a common component in emission streams, on catalytic performance was also investigated. As shown in Fig. 1b, the presence of O_2 significantly suppressed N_2O conversion for both bare Co_3O_4 and $Cu_{0.15}CoO_y$, albeit to differing degrees. For bare Co_3O_4, N_2O conversion at 500 °C dropped sharply to below 40%, reflecting its strong susceptibility to O_2 inhibition. In contrast, $Cu_{0.15}CoO_y$ maintained considerably higher activity under the same conditions, suggesting that Cu doping imparts a degree of resistance to O_2 inhibition.

Overall, these results indicate that Cu modification enhances not only the intrinsic catalytic activity but also the catalyst's ability to mitigate the inhibitory effects of O_2.

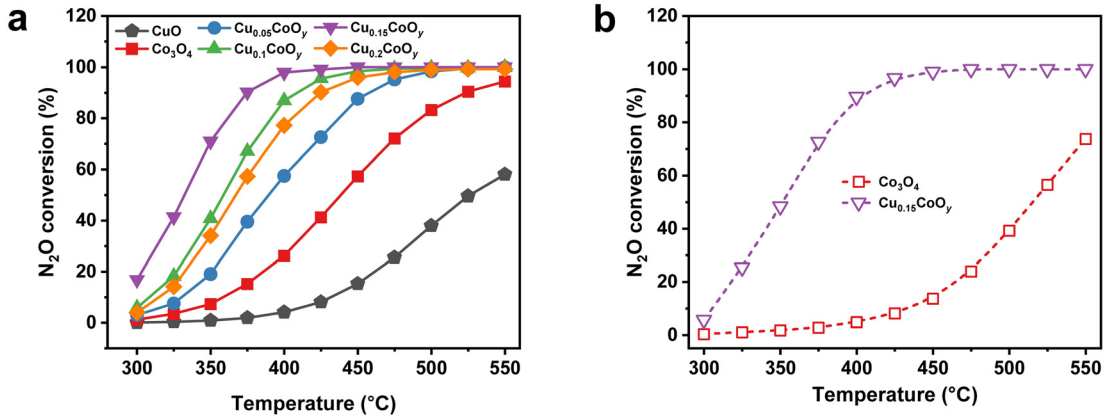

Fig. 1 N_2O decomposition performance of the Co_3O_4-based catalysts: (a) without O_2 and (b) with O_2. Reaction conditions: [N_2O] = 500 ppm, [O_2] = 5% (when used), Ar balance, flow rate = 200 mL min^{-1}, GHSV = 120 000 h^{-1}.

Further investigations are necessary to elucidate the precise contributions of Cu to the catalytic process and to validate its role as a promoter.

3.2 Textural and structural analyses

The textural properties of the bare and Cu-doped Co_3O_4 catalysts, including N_2 adsorption–desorption isotherms and resulting Brunauer–Emmett–Teller (BET) surface areas, are shown in Fig. S3† and summarized in Table 1. The data indicate that Cu incorporation increases the specific surface area.

Fig. 2a shows the XRD patterns of the bare and Cu-doped Co_3O_4 catalysts. The bare Co_3O_4 sample matches well with the cubic spinel structure (PDF no. 43-1003). Upon Cu doping, the XRD reflections remain consistent with the Co_3O_4 spinel phase, and no detectable CuO phase (PDF no. 48-1548) is observed. This absence of additional crystalline phases suggests that the doped Cu species are either (1) incorporated as isolated ions forming a homogeneous solid solution, (2) highly defective and noncrystalline, or (3) present in crystalline domains with particle sizes below the XRD detection limit. Energy-dispersive X-ray spectroscopy (EDS) mapping (Fig. S4†) further supports this view by demonstrating a uniform distribution of Co and Cu across the samples. Notably, the diffraction peak intensities gradually decrease with increasing Cu content. This trend can be primarily attributed to the reduction in crystallite size, as calculated by the Scherrer equation (Table 1).

Raman spectroscopy was employed to examine in greater detail the lattice distortions induced by Cu incorporation (Fig. 2b). All samples exhibit the characteristic Raman-active phonon modes (F^1_{2g}, E_g, F^2_{2g}, F^3_{2g}, and A_{1g}) of spinel Co_3O_4.[15,22,44] Upon Cu doping, the A_{1g} mode associated with Co^{3+}–O stretching in octahedral sites exhibits a gradual redshift, while the E_g mode corresponding to Co^{2+}–O vibrations at tetrahedral sites remains largely unchanged. Although Cu^{2+} preferentially substitutes Co^{2+} at tetrahedral (A) sites, the spinel lattice features strong coupling between tetrahedral and octahedral sublattices through shared oxygen bridges (Co–O–Co).[45] The local lattice distortions and strain introduced by Cu substitution propagate through the oxygen framework, perturbing the bonding environment of Co^{3+}–O units in octahedral sites. Moreover, due to their longer bond lengths and lower force constants, Co^{3+}–O bonds are more sensitive to lattice perturbations compared to Co^{2+}–O bonds.[46] Consequently, the A_{1g} mode undergoes a noticeable redshift upon Cu doping, while the E_g mode remains relatively stable. These results further confirm the effective incorporation of Cu into the Co_3O_4 spinel lattice and the associated structural evolution.

3.3 Surface chemical analysis

X-ray photoelectron spectroscopy (XPS) was employed to investigate the oxidation states, chemical environments, and dopant–host interactions on the catalyst surface. By analyzing the Co, Cu, and O spectra, qualitative and semi-quantitative

Table 1 The specific surface areas, crystallite sizes, and surface atomic ratios of the Co_3O_4-based catalysts

Sample	Specific surface area (m^2 g^{-1})	Crystallite size (nm)	Surface atomic ratio (%)		
			Co^{2+}/Co	Cu^{2+}/Cu	O_{ads}/O
Co_3O_4	31.9	22.9	34.0	—	46.4
$Cu_{0.05}CoO_y$	41.1	21.4	39.3	52.8	48.6
$Cu_{0.1}CoO_y$	42.7	19.1	46.0	56.4	56.7
$Cu_{0.15}CoO_y$	40.3	19.0	48.4	62.2	59.2
$Cu_{0.2}CoO_y$	38.8	18.5	43.1	56.0	50.8

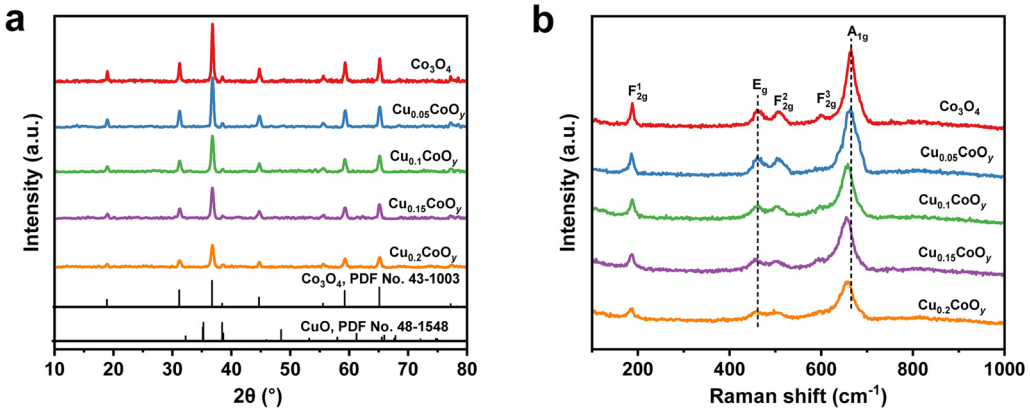

Fig. 2 XRD patterns (a) and Raman spectra (b) of the Co_3O_4-based catalysts.

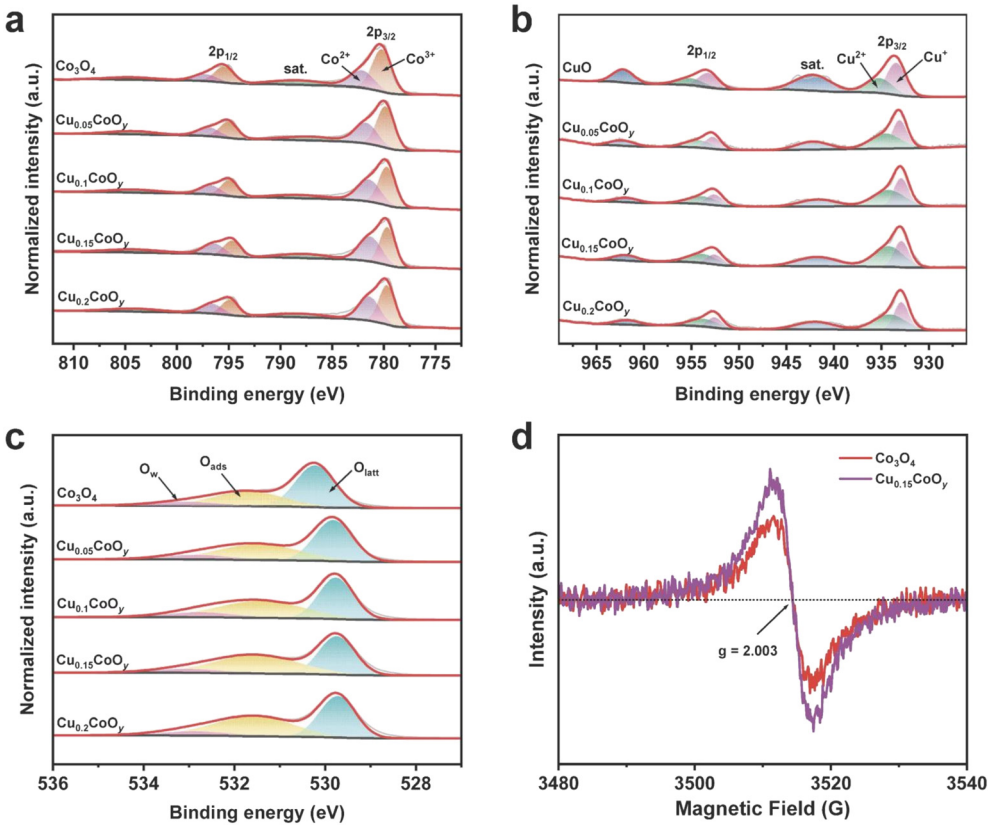

Fig. 3 XPS spectra of (a) Co 2p, (b) Cu 2p, and (c) O 1s for the Co_3O_4-based catalysts. (d) EPR spectra of the bare Co_3O_4 and $Cu_{0.15}CoO_y$ catalysts.

insights were obtained regarding elemental composition and electronic structure. The relevant XPS spectra and calculated surface compositions are shown in Fig. 3a–c and Table 1, respectively. Note that to enable a consistent comparison of the Cu 2p spectra across different samples, all XPS spectra and their deconvoluted subspectra were normalized to the maximum peak intensity of each original spectrum.

A comparison of the Co 2p and Cu 2p binding energies (BEs) reveals notable shifts to lower values in the Cu-doped samples relative to bare Co_3O_4 and CuO, indicating alterations in the electronic environment upon Cu incorporation. Deconvolution of the Co $2p_{3/2}$ peak shows two components corresponding to Co^{3+} and Co^{2+},[25,47] whereas the Cu $2p_{3/2}$ peak can be resolved into Cu^+ and Cu^{2+}.[16,48] As summarized in Table 1, the Co^{2+}/Co ratios in the Cu-doped samples exceed those of bare Co_3O_4, with the highest ratio appearing in $Cu_{0.15}CoO_y$. In parallel, the Cu^{2+}/Cu ratio increases with Cu content and likewise reaches a maximum at Cu/Co = 0.15. These observations suggest that electron transfer occurred between Cu^+ and adjacent Co^{3+} ($Co^{3+} + Cu^+ \rightarrow Co^{2+} + Cu^{2+}$) during catalyst synthesis, achieving its greatest extent at the optimal Cu doping level (0.15).

The O 1s spectra (Fig. 3c) were deconvoluted into three components: lattice oxygen (O_{latt}), adsorbed oxygen (O_{ads}), and oxygen species from adsorbed water/hydroxyl groups (O_w).[42,49,50] Notably, the amount of O_{ads} (relative to total O) increases with Cu content, peaking in $Cu_{0.15}CoO_y$, indicating that Cu doping promotes the formation of oxygen vacancies. This conclusion is further supported by EPR measurements (Fig. 3d). Both Co_3O_4 and $Cu_{0.15}CoO_y$ exhibit symmetrical signals at g = 2.003, attributed to unpaired electrons in oxygen vacancies.[51] The stronger signal intensity in $Cu_{0.15}CoO_y$ compared to bare Co_3O_4 indicates a higher concentration of such vacancies,[52] in line with the O 1s XPS results.

3.4 Redox property

The redox behavior of catalysts plays a pivotal role in N_2O decomposition, given that N_2O possesses intrinsic oxidizing characteristics.[53] Accordingly, the reducibility of the bare and Cu-doped Co_3O_4 catalysts was investigated *via* H_2-TPR, and the resulting profiles are presented in Fig. 4. For bare Co_3O_4, two distinct reduction peaks emerge at approximately 315 and 414 °C, corresponding to the sequential reduction from Co^{3+} to Co^{2+} and subsequently from Co^{2+} to Co^0.[54] Upon Cu doping, these reduction peaks shift to significantly lower temperatures, indicating enhanced reducibility. Notably, the reduction peaks associated with the Cu species overlap with those of the Co species. Among the doped samples, $Cu_{0.15}CoO_y$ exhibits the most pronounced improvement, with the first reduction peak appearing at only 175 °C. For $Cu_{0.2}CoO_y$, excess Cu forms CuO clusters, causing peaks to shift back toward higher temperatures, consistent with CuO's intrinsic reduction behavior. This clearly indicates that moderate Cu doping significantly enhances Co_3O_4 reducibility, thus boosting catalytic performance. These results suggest that Cu incorporation markedly modifies the redox properties of Co_3O_4, thereby offering a mechanistic basis for the improved N_2O decomposition performance observed in Cu-doped catalysts.

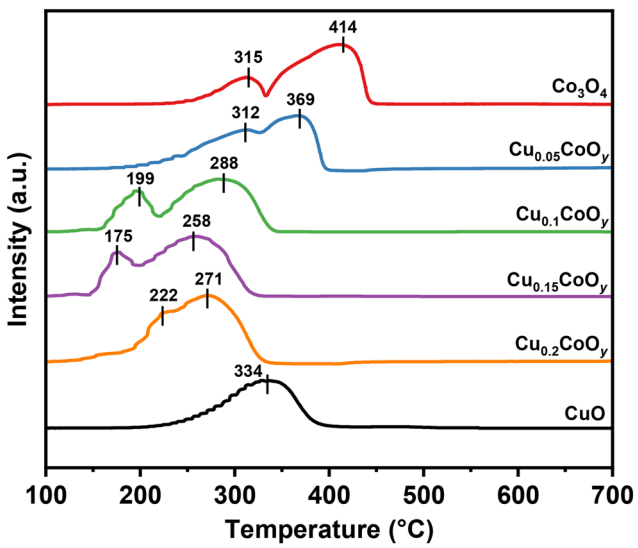

Fig. 4 H_2-TPR profiles of the CuO and Co_3O_4-based catalysts.

3.5 Identification of the intermediate species

In situ DRIFTS was conducted to identify surface-bound intermediates formed during N_2O decomposition on both bare and Cu-doped Co_3O_4 catalysts. The DRIFTS spectra and corresponding mapping results are shown in Fig. S5† and 5. A vibrational band at 2237 cm^{-1}, with a shoulder at 2207 cm^{-1}, is assigned to the N–N stretching mode of adsorbed N_2O, which was confirmed by Fig. S6.† In contrast, the band at 1422 cm^{-1} corresponds to the N–N stretching mode of *trans*-$N_2O_2^-$.[55]

Two major observations can be drawn from the DRIFTS results: (1) enhanced formation of surface species with Cu doping. The quantity of both adsorbed N_2O and *trans*-$N_2O_2^-$ species increases upon Cu incorporation, with $Cu_{0.15}CoO_y$ exhibiting the highest surface coverage. This suggests that Cu doping facilitates the chemisorption or stabilization of N_2O-derived intermediates. (2) Sequential appearance of surface intermediates. Initially, adsorbed N_2O species form on the catalyst surface; subsequently, *trans*-$N_2O_2^-$ species emerge after a brief induction period. Notably, on $Cu_{0.15}CoO_y$, the *trans*-$N_2O_2^-$ intermediate appears within approximately one minute, significantly earlier than on other catalysts, implying a faster formation pathway likely promoted by Cu doping.

Taken together, these observations strongly suggest that *trans*-$N_2O_2^-$ serves as the key intermediate in N_2O decomposition on our Co_3O_4-based catalysts. The subsequent section "3.7 identification of the predominant active site" provides additional evidence supporting its critical role in the reaction pathway.

3.6 Kinetic studies

Based on our experimental observations, we propose the following sequence of elementary steps for N_2O decomposition over the Co_3O_4-based catalysts:

$$N_2O(g) + * \overset{K_1}{\leftrightarrow} N_2O* \quad (R5)$$

$$N_2O* \overset{k_2}{\rightarrow} N_2(g) + O* \quad (R6)$$

$$N_2O(g) + O* \overset{K_3}{\leftrightarrow} N_2O_2^* \quad (R7)$$

$$N_2O_2^* \overset{k_4}{\rightarrow} O_2^* \quad (R8)$$

$$O_2^* \overset{k_5}{\rightarrow} N_2(g) + * \quad (R9)$$

where * denotes a vacant active site.

Two elementary steps, namely, the splitting of adsorbed N_2O (R6) and the desorption of O_2 (R9), are commonly

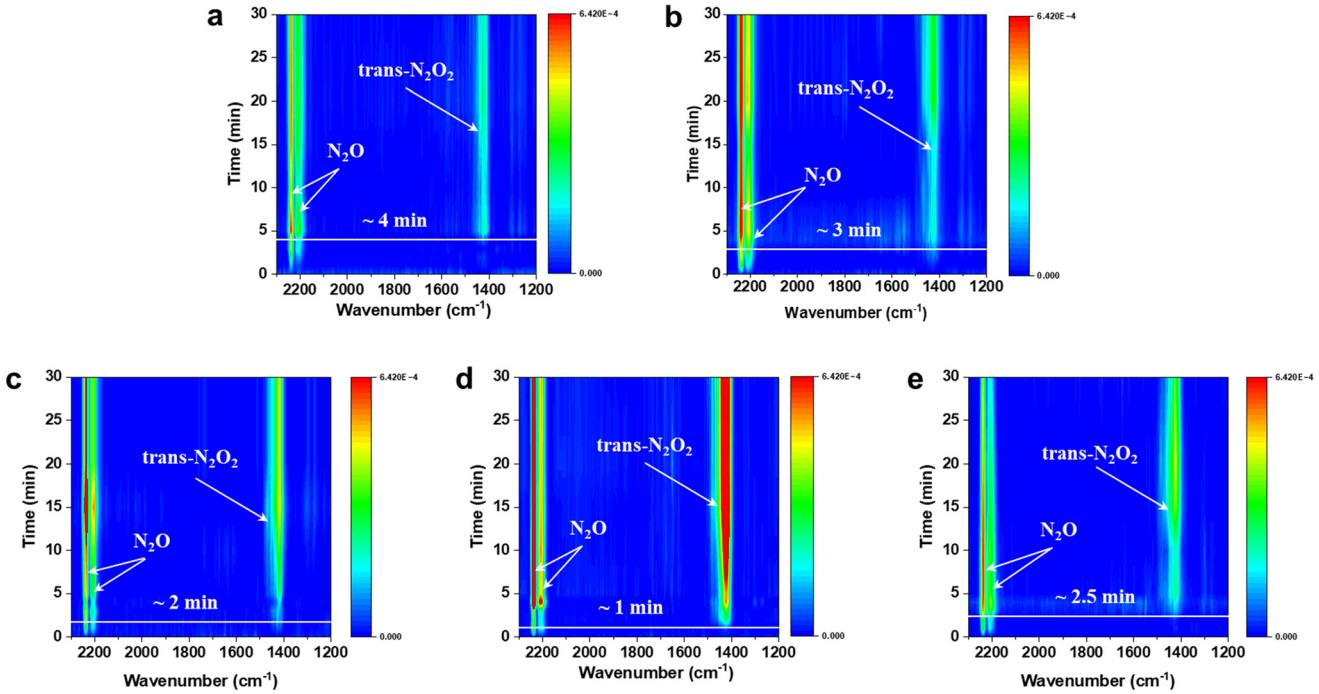

Fig. 5 *In situ* DRIFTS mapping results of N_2O decomposition (a) Co_3O_4, (b) $Cu_{0.05}CoO_y$, (c) $Cu_{0.1}CoO_y$, (d) $Cu_{0.15}CoO_y$, and (e) $Cu_{0.2}CoO_y$ catalysts at 325 °C for 30 min.

proposed as potential rate-determining steps (RDS) in N_2O decomposition over metal oxide catalysts.[16,56–58] To clarify this, we carried out kinetic modeling based on both hypotheses.

Assuming that R6 is the RDS, the rate of N_2O decomposition is:

$$r_{N_2O} = k_2[N_2O^*] \quad (3)$$

If R5 is quasi-equilibrated, then:

$$[N_2O^*] = K_1[N_2O(g)][^*] \quad (4)$$

Substituting eqn (4) into eqn (3):

$$r_{N_2O} = k_2K_1[N_2O(g)][^*] \quad (5)$$

Under steady-state conditions and assuming the concentration of active sites [*] remains approximately constant due to continuous regeneration through oxygen removal, the rate expression simplifies to:

$$r_{N_2O} = k_{eff}[N_2O(g)] \quad (6)$$

where k_{eff} is an apparent rate constant for N_2O decomposition (mol g^{-1} min^{-1}).

Thus, the reaction is expected to exhibit first-order kinetics with respect to N_2O.

If O_2 desorption (R9) is the RDS, the overall reaction rate is:

$$r_{N_2O} = k_5[O_2^*] \quad (7)$$

From (R8) (assumed fast), we have:

$$[O_2^*] = k_4[N_2O_2^*] \quad (8)$$

From (R7) (equilibrium):

$$[N_2O_2^*] = K_3[N_2O][O^*] \quad (9)$$

From (R6) (fast step):

$$[O^*] = k_2[N_2O^*] \quad (10)$$

From (R5) (equilibrium):

$$[N_2O^*] = K_1[N_2O(g)][^*] \quad (11)$$

Substituting eqn (10) and (11) into eqn (9):

$$[N_2O_2^*] = K_3[N_2O(g)](k_2K_1[N_2O(g)][^*]) = k_2K_1K_3[N_2O(g)]^2[^*] \quad (12)$$

Substituting into eqn (8):

$$[O_2^*] = k_4k_2K_1K_3[N_2O(g)]^2[^*] \quad (13)$$

Substituting into eqn (7):

$$r_{N_2O} = k_5 k_4 k_2 K_1 K_3 [N_2O(g)]^2 [*] \quad (14)$$

Now, we estimate [*] based on the site balance. Assuming that only N_2O, O*, and * significantly occupy the surface:

$$L = [*] + [N_2O*] + [O*] \quad (15)$$

Using eqn (10) and (11):

$$L = [*](1 + K_1[N_2O(g)](1 + k_2)) \quad (16)$$

Thus:

$$[*] = \frac{L}{1 + K_1[N_2O(g)](1 + k_2)} \quad (17)$$

Substituting [*] back into the rate expression:

$$r_{N_2O} = \frac{L k_5 k_4 k_2 K_1 K_3 [N_2O(g)]^2}{1 + K_1[N_2O(g)](1 + k_2)} \quad (18)$$

This rate law clearly shows a nonlinear dependence on $[N_2O]$, approximately second-order at low concentrations.

The experimentally observed first-order kinetics (Fig. 6a–e) contradict the rate law derived under the assumption that R9 is rate-limiting. Therefore, (R9) (O_2 desorption) can be excluded as the rate-determining step. Instead, the observed linear correlation between N_2O concentration and decomposition rate across all catalysts supports the conclusion that (R6) (N_2O dissociation) is the primary rate-determining step under the studied conditions.

3.7 Identification of the predominant catalytic site

As evidenced by the catalytic performance (Fig. 1a) and XPS results (Table 1), Cu cations can be effectively ruled out as the primary active sites in Cu-doped Co_3O_4 catalysts. Instead, Cu appears to function as an electronic structure promoter, regulating the surface concentration of Co^{2+} and oxygen vacancies rather than acting as an independent active site. Accordingly, the focus shifts to determining whether Co^{2+} or Co^{3+} on the catalyst surface serves as the main active site for N_2O decomposition.

Linear regression analysis of the kinetic data (Fig. 6a–e) provided the apparent reaction rate constants (k_{eff}), as shown in Fig. 7a. According to eqn (5) and (6), k_{eff} is directly proportional to the N_2O adsorption equilibrium constant (K_1), the N_2O dissociation rate constant (k_2), and the concentration of active sites (*). Although K_1 is known to decrease with increasing temperature, k_{eff} increases for all catalysts. To evaluate the effect of the declining K_1 on k_{eff}, we determined the activation energy (E_a) from both the k_{eff} data and the overall reaction rate. As illustrated in Fig. 7b and c, the comparable E_a values obtained by these two methods indicate that the temperature-induced decrease in K_1 has a negligible impact on k_{eff}.

In addition, the N_2O dissociation rate constant k_2 is influenced by catalyst reducibility, while the number of available active sites (*) is predominantly determined by the concentration of low-valence surface cations.[58] H_2-TPR data (Fig. 4) indicate that catalyst reducibility follows the trend: $Cu_{0.15}CoO_y$ > $Cu_{0.1}CoO_y$ > $Cu_{0.2}CoO_y$ > $Cu_{0.05}CoO_y$ > Co_3O_4. Concurrently, XPS results show that the fraction

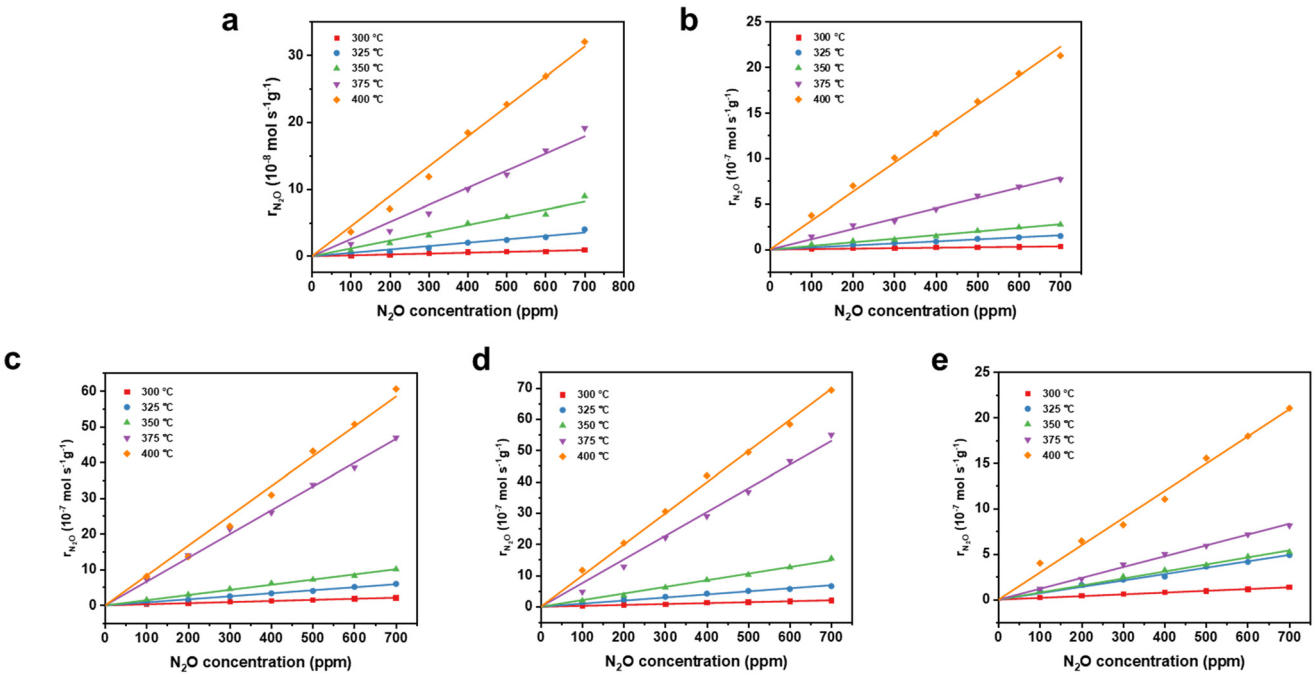

Fig. 6 Dependence of N_2O decomposition rate on N_2O concentration over (a) Co_3O_4, (b) $Cu_{0.05}CoO_y$, (c) $Cu_{0.1}CoO_y$, (d) $Cu_{0.15}CoO_y$, and (e) $Cu_{0.2}CoO_y$ catalysts.

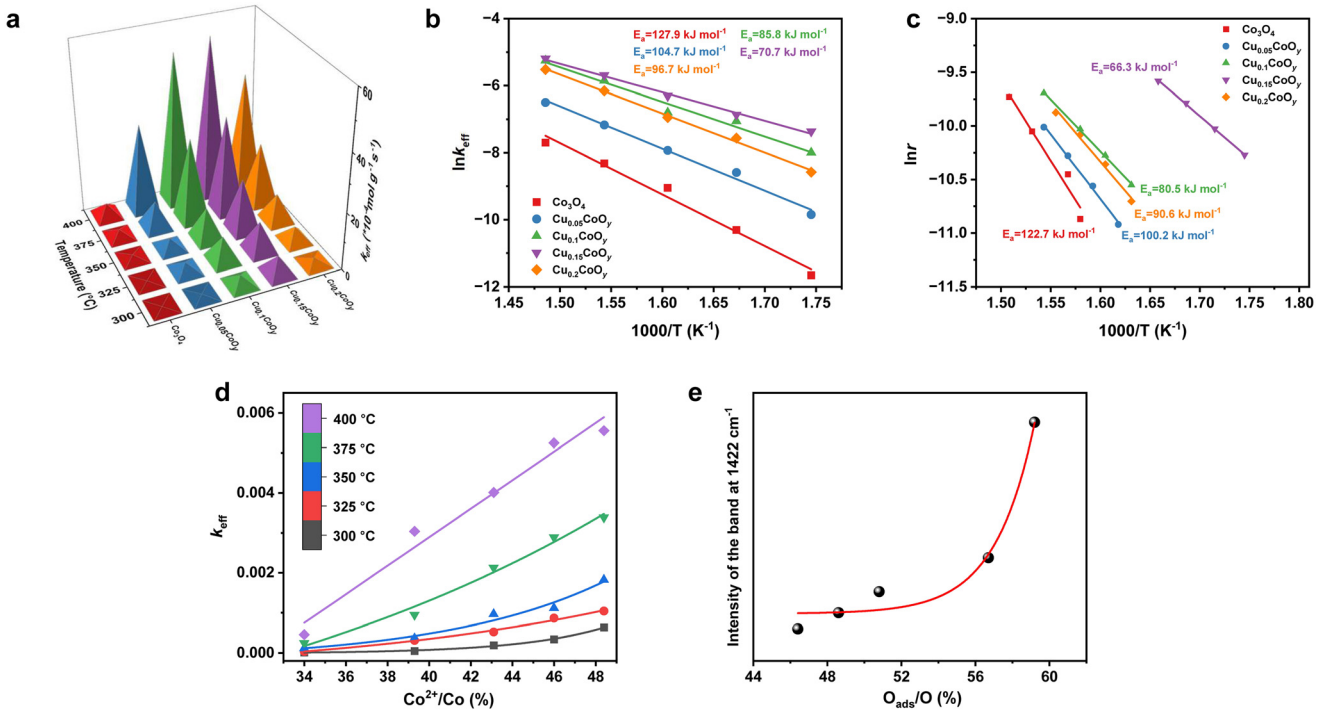

Fig. 7 (a) N_2O decomposition rate constants (k_{eff}) of the Co_3O_4-based catalysts. (b) Arrhenius plots for N_2O decomposition based on k_{eff}. (c) Arrhenius plots for N_2O decomposition derived from the reaction rate of r_{N_2O} calculated by eqn (2). (d) Correlation between the rate constant and the molar ratio of Co^{2+}/Co. (e) Correlation between the intensity of the IR band at 1422 cm^{-1} and the molar ratio of O_{ads}/O.

of surface Co^{2+} mirrors this sequence. These observations collectively suggest that Co^{2+} cations act as the predominant active sites for N_2O decomposition. To reinforce this conclusion, Fig. 7d plots k_{eff} *versus* the molar ratio of Co^{2+}/Co at different reaction temperatures, revealing a positive correlation. Thus, Co^{2+} clearly emerges as the principal active site driving N_2O decomposition on our Co_3O_4-based catalysts.

The role of oxygen vacancies cannot be overlooked. We have now confirmed that Co^{2+} cation is indeed the principal active site. Therefore, according to reaction (R6), N_2O is initially adsorbed onto this Co^{2+} site, where it subsequently dissociates to yield gaseous N_2 and atomic oxygen. The former readily desorbs, whereas the latter cannot remain stably bound to the Co^{2+} cation and thus migrates to nearby oxygen vacancies *via* oxygen spillover. To verify this hypothesis, we performed DFT calculations (Fig. S7 and S8, Tables S1 and S2†), which confirm that the oxygen atom produced by dissociation spontaneously migrates to the oxygen vacancy adjacent to the Co^{2+} cation. Furthermore, Cu doping facilitates this process. EPR results (Fig. 3d) reveal that oxygen vacancies possess localized negative charges, which stabilize the dissociated oxygen as O^- species. The subsequent reaction between O^- and a second N_2O molecule is hypothesized to form the *trans*-$N_2O_2^-$ intermediate, which is further supported by the strong correlation between the intensity of the 1422 cm^{-1} IR band (Fig. S5†) and adsorbed oxygen concentration (Table 1) on the catalyst surface (Fig. 7e). This also underscore the pivotal role of *trans*-$N_2O_2^-$ as a key intermediate in the N_2O decomposition pathway.

Based on these findings, we propose that the Co^{2+} cation and a neighboring oxygen vacancy jointly constitute the active center in the form of a "⊡-Co^{2+}" pair (where "⊡" denotes an oxygen vacancy, O_v).

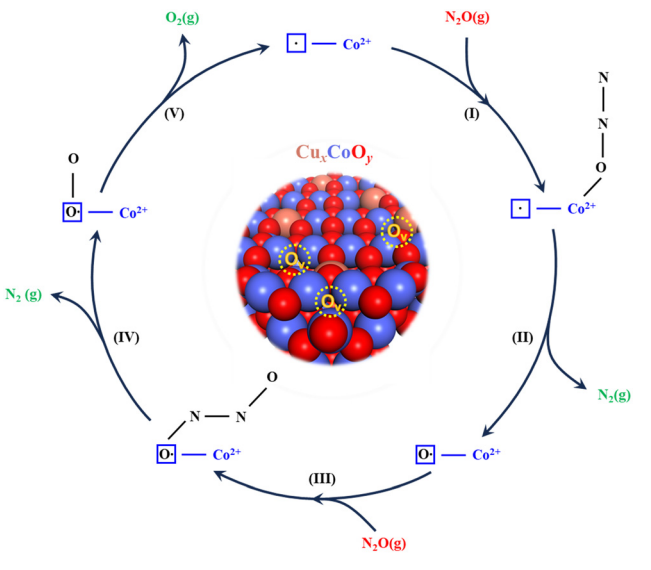

Scheme 1 Proposed reaction mechanism of N_2O decomposition over Co-based catalysts.

3.8 Possible reaction mechanism

Based on the foregoing results, we propose a plausible mechanism for N_2O decomposition on Co_3O_4-based catalysts (Scheme 1). During catalyst preparation, "⊡-Co^{2+}" pairs, consisting of a Co^{2+} cation and a neighboring oxygen vacancy, are formed, with Cu doping significantly increasing their abundance. The catalytic cycle initiates with N_2O adsorption on the Co^{2+} site, followed by dissociation into N_2(g) and a dissociated oxygen atom (I). The atomic oxygen then migrates from the Co^{2+} site to fill the nearby oxygen vacancy *via* oxygen spillover (II). In the next step, a second N_2O molecule reacts with the adsorbed oxygen, forming the *trans*-$N_2O_2^-$ intermediate (III), which subsequently decomposes into N_2(g) and adsorbed O_2 (IV). Finally, the adsorbed O_2 desorbs from the oxygen vacancy (V), regenerating the "⊡-Co^{2+}" pair and completing the catalytic cycle.

4. Conclusions

In summary, we successfully developed Cu-doped Co_3O_4 spinel catalysts using a surface modification strategy, achieving remarkable N_2O decomposition performance. Precise Cu doping enhanced the surface concentration of Co^{2+} cations and oxygen vacancies, significantly improving the catalysts' redox properties, as confirmed by morphological, XPS, and H_2-TPR analyses. Kinetic studies combined with DFT calculations identified the "⊡-Co^{2+}" pair, composed of a Co^{2+} cation and an adjacent oxygen vacancy, as the intrinsic active center for N_2O decomposition. Importantly, *in situ* DRIFTS provided the first direct evidence of *trans*-$N_2O_2^-$ as a critical intermediate species formed on this active center, playing a key role in the catalytic pathway. Building on these findings, we proposed a detailed reaction mechanism in which N_2O first adsorbs and dissociates on the Co^{2+} anion of a "⊡-Co^{2+}" pair. The resulting atomic oxygen migrates *via* oxygen spillover to the oxygen vacancy within the same "⊡-Co^{2+}" pair, facilitating the formation of *trans*-$N_2O_2^-$ and driving the catalytic cycle to completion. These findings address key uncertainties in the catalytic behavior of spinel oxides and offer a robust framework for the rational design of advanced catalysts with improved efficiency and selectivity. Beyond N_2O abatement, this approach can inspire the development of oxide catalysts for broader environmental and industrial applications.

Data availability

The original data are available from the corresponding author on reasonable request.

Author contributions

Y. Z. and T. Z. designed the experiments, evaluated the catalytic performance, carried out the structural characterizations, and wrote the manuscript. Q. D. and J. Z. helped with the DFT calculations, data analysis and paper writing. T. Z. and J. L. reviewed and revised the manuscript.

Conflicts of interest

The authors declare no conflicts of interest.

Acknowledgements

This work was financially supported by the National Natural Science Foundation of China (22176216), the National Engineering Laboratory for Mobile Source Emission Control Technology (NELMS2020A13), and the Basic Research Fund of Zhongye Changtian International Engineering Co., Ltd. (2021JCYJ05).

References

1 M. Konsolakis, *ACS Catal.*, 2015, **5**, 6397–6421.
2 X. Wang, R. Duan, Z. Li, M. Gao, Y. Fu, Y. Han, G. He and H. He, *Environ. Sci. Technol.*, 2025, **59**, 5839–5847.
3 Z. Hu, J. W. Lee, K. Chandran and S. Kim, *Environ. Sci. Technol.*, 2012, **46**, 6470–6480.
4 I. Song, Y. Wang, J. Szanyi and K. Khivantsev, *Appl. Catal., B*, 2024, **343**, 1–7.
5 A. Dandekar and M. A. Vannice, *Appl. Catal., B*, 1999, **22**, 179–200.
6 M. Piumetti, M. Hussain, D. Fino and N. Russo, *Appl. Catal., B*, 2015, **165**, 158–168.
7 S. Parres-Esclapez, I. Such-Basañez, M. J. Illán-Gómez, C. Salinas-Martínez De Lecea and A. Bueno-López, *J. Catal.*, 2010, **276**, 390–401.
8 Y. Jing, K. Taketoshi, N. Zhang, C. He, T. Toyao, Z. Maeno, T. Ohori, N. Ishikawa and K. I. Shimizu, *ACS Catal.*, 2022, **12**, 6325–6333.
9 C. Ohnishi, K. Asano, S. Iwamoto, K. Chikama and M. Inoue, *Catal. Today*, 2007, **120**, 145–150.
10 F. Kapteijn, J. Rodriguez-Mirasol and J. A. Moulijn, *Appl. Catal., B*, 1996, **9**, 25–64.
11 N. Richards, J. H. Carter, L. A. Parker, S. Pattisson, D. G. Hewes, D. J. Morgan, T. E. Davies, N. F. Dummer, S. Golunski and G. J. Hutchings, *ACS Catal.*, 2020, **10**, 5430–5442.
12 F. Lin, T. Andana, Y. Wu, J. Szanyi, Y. Wang and F. Gao, *J. Catal.*, 2021, **401**, 70–80.
13 T. Zhang, Y. Qiu, G. Liu, J. Chen, Y. Peng, B. Liu and J. Li, *J. Catal.*, 2020, **392**, 322–335.
14 B. M. Abu-Zied, W. Schwieger and A. Unger, *Appl. Catal., B*, 2008, **84**, 277–288.
15 Y. Gong, Z. Liu, Z. Li, C. Liu, N. Yan and L. Ma, *Environ. Sci. Technol.*, 2024, **58**, 906–914.
16 S. Xiong, J. Chen, N. Huang, S. Yang, Y. Peng and J. Li, *Environ. Sci. Technol.*, 2019, **53**, 10379–10386.
17 C. Shan, Y. Wang, J. Li, Q. Zhao, R. Han, C. Liu and Q. Liu, *Environ. Sci. Technol.*, 2023, **57**, 9495–9514.
18 K. Asano, C. Ohnishi, S. Iwamoto, Y. Shioya and M. Inoue, *Appl. Catal., B*, 2008, **78**, 242–249.

19 H. Yu, M. Tursun, X. Wang and X. Wu, *Appl. Catal., B*, 2016, **185**, 110–118.
20 Y. Wang, K. Zheng, X. Hu, W. Zhou, X. Wei and Y. Zhao, *Mol. Catal.*, 2019, **470**, 104–111.
21 J. Sun, L. Wang, L. Zhang, Y. Zhao, Y. Chi, H. Wang, C. Li, J. Liu and J. Liu, *ACS Appl. Energy Mater.*, 2021, **4**, 8496–8505.
22 H. Liu, S. Yang, G. Wang, H. Liu, Y. Peng, C. Sun, J. Li and J. Chen, *Environ. Sci. Technol.*, 2022, **56**, 16325–16335.
23 B. Li, X. Duan, T. Zhao, B. Niu, G. Li, Z. Zhao, Z. Yang, D. Liu, F. Zhang, J. Cheng and Z. Hao, *Environ. Sci. Technol.*, 2024, **58**, 2153–2161.
24 H. Yu and X. Wang, *Catal. Commun.*, 2018, **106**, 40–43.
25 Y. Xiong, Y. Zhao, X. Qi, J. Qi, Y. Cui, H. Yu and Y. Cao, *Environ. Sci. Technol.*, 2021, **55**, 13335–13344.
26 P. Stelmachowski, G. Maniak, J. Kaczmarczyk, F. Zasada, W. Piskorz, A. Kotarba and Z. Sojka, *Appl. Catal., B*, 2014, **146**, 105–111.
27 T. Franken and R. Palkovits, *Appl. Catal., B*, 2015, **176–177**, 298–305.
28 G. Grzybek, P. Stelmachowski, S. Gudyka, P. Indyka, Z. Sojka, N. Guillén-Hurtado, V. Rico-Pérez, A. Bueno-López and A. Kotarba, *Appl. Catal., B*, 2016, **180**, 622–629.
29 Z. Zhuang, B. Guan, J. Chen, C. Zheng, J. Zhou, T. Su, Y. Chen, C. Zhu, X. Hu, S. Zhao, J. Guo, H. Dang, Y. Zhang, Y. Yuan, C. Yi, C. Xu, B. Xu, W. Zeng, Y. Li, K. Shi, Y. He, Z. Wei and Z. Huang, *Chem. Eng. J.*, 2024, **486**, 150374.
30 X. Liu, G. Qiu and X. Li, *Nanotechnology*, 2005, **16**, 3035–3040.
31 K. Shojaee, A. Montoya and B. S. Haynes, *Comput. Mater. Sci.*, 2013, **72**, 15–25.
32 Y. Maimaiti, M. Nolan and S. D. Elliott, *Phys. Chem. Chem. Phys.*, 2014, **16**, 3036–3046.
33 G. Kresse and J. Furthmüller, *Comput. Mater. Sci.*, 1996, **6**, 15–50.
34 G. Kresse and J. Furthmüller, *Phys. Rev. B: Condens. Matter Mater. Phys.*, 1996, **54**, 11169–11186.
35 P. E. Blöchl, *Phys. Rev. B: Condens. Matter Mater. Phys.*, 1994, **50**, 17953–17979.
36 G. Kresse and D. Joubert, *Mater. Today Phys.*, 1999, **59**, 1758–1775.
37 J. P. Perdew and K. Burke, *Phys. Rev. Lett.*, 1996, **77**, 3865–3868.
38 B. X. Yang, L. P. Ye, H. J. Gu, J. H. Huang, H. Y. Li and Y. Luo, *J. Mol. Model.*, 2015, **21**, 1–7.
39 F. Zasada, W. Piskorz and Z. Sojka, *J. Phys. Chem. C*, 2015, **119**, 19180–19191.
40 S. Grimme, J. Antony, S. Ehrlich and H. Krieg, *J. Chem. Phys.*, 2010, **132**, 154104.
41 F. Zasada, W. Piskorz, J. Janas, J. Grybos, P. Indyka and Z. Sojka, *ACS Catal.*, 2015, **5**, 6879–6892.
42 F. Zasada, J. Janas, W. Piskorz, M. Gorczynska and Z. Sojka, *ACS Catal.*, 2017, **7**, 2853–2867.
43 L. Nowakowski, C. Hudy, F. Zasada, J. Gryboś, W. Piskorz, A. Wach, Y. Kayser, J. Szlachetko and Z. Sojka, *J. Am. Chem. Soc.*, 2024, **146**, 24450–24466.
44 L. He, Z. Li and Z. Zhang, *Nanotechnology*, 2008, **19**, 15–19.
45 X. Wang, Y. Liu, T. Zhang, Y. Luo, Z. Lan, K. Zhang, J. Zuo, L. Jiang and R. Wang, *ACS Catal.*, 2017, **7**, 1626–1636.
46 R. D. Shannon, *Acta Crystallogr., Sect. A*, 1976, **32**, 751–767.
47 J. Bae, D. Shin, H. Jeong, B. S. Kim, J. W. Han and H. Lee, *ACS Catal.*, 2019, **9**, 10093–10100.
48 M. Zhou, L. Cai, M. Bajdich, M. García-Melchor, H. Li, J. He, J. Wilcox, W. Wu, A. Vojvodic and X. Zheng, *ACS Catal.*, 2015, **5**, 4485–4491.
49 H. Liu, J. Chen, Y. Wang, S. Xiong, Z. Su, Y. Wang, W. Yang, X. Chu, W. Yang, Y. Peng, W. Si and J. Li, *Chem. Eng. J.*, 2021, **414**, 128643.
50 Y. Liu, H. Dai, J. Deng, S. Xie, H. Yang, W. Tan, W. Han, Y. Jiang and G. Guo, *J. Catal.*, 2014, **309**, 408–418.
51 T. Zhang, G. Ma, Y. Mu, J. Li, Y. Peng, G. H. Liu, B. Liu, J. Chen and J. Li, *ACS EST Eng.*, 2023, **3**, 1394–1401.
52 S. Cai, H. Hu, H. Li, L. Shi and D. Zhang, *Nanoscale*, 2016, **8**, 3588–3598.
53 L. Xue, C. Zhang, H. He and Y. Teraoka, *Appl. Catal., B*, 2007, **75**, 167–174.
54 A. Parastaev, V. Muravev, E. H. Osta, A. J. F. van Hoof, T. F. Kimpel, N. Kosinov and E. J. M. Hensen, *Nat. Catal.*, 2020, **3**, 526–533.
55 K. I. Hadjiivanov, *Catal. Rev.:Sci. Eng.*, 2000, **42**, 71–144.
56 T. Yamashita and A. Vannice, *J. Catal.*, 1996, **161**, 254–262.
57 P. J. Smeets, B. F. Sels, R. M. van Teeffelen, H. Leeman, E. J. M. Hensen and R. A. Schoonheydt, *J. Catal.*, 2008, **256**, 183–191.
58 L. Wu, W. Qin, X. Hu, S. Ju, C. Dong and Y. Yang, *Surf. Sci.*, 2015, **632**, 83–87.